IEEE Access
Multidisciplinary | Rapid Review | Open Access Journal

Received June 26, 2019, accepted July 22, 2019, date of publication July 29, 2019, date of current version August 20, 2019.

Digital Object Identifier 10.1109/ACCESS.2019.2931515

Force/Torque Sensorless Compliant Control Strategy for Assembly Tasks Using a 6-DOF Collaborative Robot

FAN ZENG, (Student Member, IEEE), JULIANG XIAO, (Member, IEEE), AND HAITAO LIU, (Member, IEEE)

Key Laboratory of Mechanism Theory and Equipment Design of Ministry of Education, Tianjin University, Tianjin 300350, China

Corresponding author: Juliang Xiao (tjxjl@ tju.edu.cn)

This work was supported in part by the National Natural Science Foundation of China under Grant 51721003, Grant 51622508, and Grant 91648202.

ABSTRACT The flexibility of the robot assembly process is critical, and a robot assembly system that is not flexible may damage the workpieces. Most researchers make the assembly process flexible by installing a six-dimensional force/torque sensor at the end of robots, but doing so will result in an increase in the costs of the robotic assembly system. To this end, this paper proposes an external force/torque calculation algorithm based on dynamic model identification to replace the six-dimensional force/torque sensor; the algorithm can reduce the costs while achieving a flexible assembly. In this paper, the impedance model of the environment and the dynamic model of the robot with friction are unified. Based on the unified model, the virtual contact surface is proposed to optimize the assembly. To ensure the accuracy of the assembly, the compliant control method of this paper uses the PD-based position control as the control inner loop and the impedance control as the control outer loop. To verify the accuracy of the compliant control method, a 6-DOF series collaborative robot which is developed in our laboratory is used to complete the peg-in-hole assembly experiment. The experimental results show that the algorithm has good flexibility and positional accuracy.

INDEX TERMS Collaborative robot, compliant control, impedance control, virtue contact surface, model identification, flexible assembly.

I. INTRODUCTION

With the development of the 3C industry which stands for Computer, Communication and Consumer Electronic, the demand for its products is constantly increasing as well. The 3C manufacturing industry mainly includes four aspects: parts production, assembly, inspection, and packaging [1]. Many scholars [2],[3] have established assembly models and studied assembly process of industries. These industries have many types of products and are generally small in size. Small, lightweight and flexible collaborative robots are better choices than traditional bulky industrial robots. These lightweight collaborative robots often need to collaborate with people to undertake a large number of handling and assembly jobs. Currently, drag teaching is a standard function of collaborative robots. When the operator drags the collaborative robot to complete the assembly task, it is difficult to ensure that the two workpieces are fully mated. Therefore, the flexibility of the robot in the assembly is crucial, and an inflexible robot may damage the assembled product. To this end, this paper proposes a compliant control strategy without a force/torque sensor (FTS) to make the collaborative robot have human-like flexibility in completing the assembly tasks.

To ensure the flexibility of the robot during assembly, compliant control is widely used. There are two main ways to achieve compliant control. The first is passive compliant control. The robot relies on some auxiliary compliant mechanism to make it naturally adaptable to external forces when it comes into contact with the workpieces. Park *et al.* [4] uses a passive compliant mechanism to complete the assembly task, and Zhao *et al.* [5] proposes an impedance control method for series elastic actuators. However, this kind of joint cannot eliminate the contradiction between the high stiffness and

The associate editor coordinating the review of this manuscript and approving it for publication was Shun-Feng Su.

high flexibility of the robot. Additionally, controlling this joint may require adding some additional sensors and this will increase the complexity of the control system. The second is active compliant control. The robot uses the force feedback to actively control the force using a certain control strategy. The most common active compliant control methods are force/position hybrid control and impedance control. Yoshikawa [6], Raibert and Craig [7], and Khatib [8] use the force/position hybrid control to control the force and position separately. To ensure the flexibility of the robot during the assembly process, position control and force control are required to be switched back and forth, which can easily cause instability and poor real-time problems and cannot meet the assembly needs. At present, many scholars [9]–[11] have studied the impedance control of robots. Impedance control was first proposed by Hogan [12] in 1985. Impedance control is different from force/position hybrid control. It is a method for controlling the stiffness, damping and inertia of the robot, and thus the control of the dynamic relationship between its end force, displacement, velocity and acceleration can be achieved. Impedance control is one of the most stable methods of controlling the interaction process, which makes impedance control very suitable for assembly tasks. However, pure impedance control cannot ensure that the robot can perform assembly tasks accurately.

To ensure the flexibility of the robot, it is also necessary to observe the contact force/torque of the robot end-effector with the external environment in real time. The FTS accurately detects the contact force and thus helps to compensate for the positional uncertainty of the object [13]. Therefore, most researchers [14]–[16] on impedance control have installed expensive six-dimensional FTSs on the robot to detect the external force. However, the FTS is easily damaged, which makes their use and maintenance costs high. Xiao *et al.* [17] uses an external force/torque observer based on generalized momentum to calculate the external force at the end-effector of the robot. Flores-Abad [18] constructed a disturbance of observer (DOB) for impedance control, but our experimental results show that these kinds of external torque observers cannot accurately calculate the external force/torque and they cannot be used for control. Chan and Liaw [19] and Krüger *et al.* [20] apply impedance control to robot assembly. Their method is to feed back the contact force between the robot end-effector and the assembled component in order to achieve flexible assembly. However, their method can easily scratch and damage the assembled parts when assembling the easily worn workpieces.

To solve these problems, this paper proposes a sensorless compliant control method for a 6 degrees of freedom (DOF) tandem rigid robot combining mature position control with impedance control. Position control is used as the inner loop, and impedance control is used as the outer loop to ensure that the robot can accurately complete the assembly task. When assembling the easily worn workpieces, there is a large contact force and impact force between the workpieces and the end-effector, which easily damages the surfaces of the parts. For this reason, a virtual contact surface (VCS) is proposed in order to optimize the assembly. To replace the expensive six-dimensional FTS, this paper identifies the dynamic model of the robot, and proposes a nonlinear friction model as secondary compensation to improve the accuracy of the dynamic model.

The structure of this paper is organized as follows. The dynamic model and impedance model of robot and the VCS model are established in Section II. The calculation algorithm of the external force/torque of the robot end-effector in Cartesian space is described in Section III. In Section IV, a compliant control method without FTS is proposed and the peg-in-hole assembly model is analyzed in detail. In Section V, the proposed compliant control method is verified through a peg-in-hole experiment by the laboratory-designed 6-DOF collaborative robot.

II. MODELING

A. DYNAMIC MODEL OF ROBOT

Obtaining the accurate dynamic model of the robot is crucial for the subsequent establishment of the compliant control algorithm. The accuracy of the dynamic model directly affects the compliant control. For n-DOF series rigid robots, there are generally transmissions and harmonic reducers in the joints, and there is a large friction torque. Therefore, the frictional torque of the joints cannot be ignored. The dynamic equation of the robot in the joint space can be written as

$$\boldsymbol{M}(\boldsymbol{q})\ddot{\boldsymbol{q}} + \boldsymbol{C}(\boldsymbol{q}, \dot{\boldsymbol{q}})\dot{\boldsymbol{q}} + \boldsymbol{G}(\boldsymbol{q}) + \boldsymbol{F}_f(\boldsymbol{q}, \dot{\boldsymbol{q}}) = \boldsymbol{\tau}_d - \boldsymbol{\tau}_e \quad (1)$$

where $\boldsymbol{M}(\boldsymbol{q}) \in \mathbf{R}^{n\times n}$ is the symmetric inertia matrix; $\boldsymbol{C}(\boldsymbol{q}, \dot{\boldsymbol{q}}) \in \mathbf{R}^{n\times n}$ is the Coriolis and centrifugal force matrix, $\boldsymbol{G}(\boldsymbol{q}) \in \mathbf{R}^{n\times n}$ is the vector of the gravitational torques; $\boldsymbol{F}_f(\boldsymbol{q}, \dot{\boldsymbol{q}}) \in \mathbf{R}^{n\times n}$ is the frictional torque; $\boldsymbol{q}$, $\dot{\boldsymbol{q}}$, and $\ddot{\boldsymbol{q}}$ are $n \times 1$ vectors, including the angular displacement, angular velocity and angular acceleration of joints in the joint space, respectively; $\boldsymbol{\tau}_d \in \mathbf{R}^{n\times 1}$ is the driving torque of joints; and $\boldsymbol{\tau}_e \in \mathbf{R}^{n\times 1}$ is the disturbing torque generated by the external environment to the robot. Furthermore,

$$\boldsymbol{\tau}_e = \boldsymbol{J}^T \boldsymbol{F}_e \quad (2)$$

where $\boldsymbol{F}_e \in \mathbf{R}^{6\times 1}$ is the external force that is applied to the robot by the environment, and $\boldsymbol{J} \in \mathbf{R}^{n\times n}$ is the Jacobian matrix. For establishing the dynamic model of robot, we assumed that the residual torques caused by the gravity gradient, air drag and magnetic forces are expected to be much smaller in comparison to the robots actuator torques, inertia torques and friction torques.

B. IMPEDANCE MODEL OF ROBOT

The impedance for the robot controls the dynamic relationship between the end force, displacement, velocity and acceleration by controlling the stiffness, damping and inertia of the robot. The end-effector of a robot has both translation and

rotation during the assembly process, and so the impedance models of the translation and rotation are established separately. To meet the control requirements, we usually use the second-order linear equation to express the impedance characteristics of the end-effector [21].

First, considering the external forces $\boldsymbol{f}_e$ of the end-effector, the impedance characteristic between the actual position and the reference position of the end-effector can be described by

$$\boldsymbol{M}_p(\ddot{\boldsymbol{p}} - \ddot{\boldsymbol{p}}_d) + \boldsymbol{B}_p(\dot{\boldsymbol{p}} - \dot{\boldsymbol{p}}_d) + \boldsymbol{K}_p(\boldsymbol{p} - \boldsymbol{p}_d) = \boldsymbol{f}_e \tag{3}$$

where $\boldsymbol{p}$ is the actual position of the end-effector; $\boldsymbol{p}_d$ is the reference position of the end-effector; and $\boldsymbol{M}_p$, $\boldsymbol{B}_p$, and $\boldsymbol{K}_p$ are the inertia diagonal matrix, the damping diagonal matrix and the stiffness diagonal matrix of the robot corresponding to the translation, respectively.

Then, considering the external torque $\boldsymbol{\mu}_e$, the impedance characteristic between the actual orientation and the reference orientation of the end-effector can be described by

$$\boldsymbol{M}_\varphi(\ddot{\boldsymbol{\varphi}} - \ddot{\boldsymbol{\varphi}}_d) + \boldsymbol{B}_\varphi(\dot{\boldsymbol{\varphi}} - \dot{\boldsymbol{\varphi}}_d) + \boldsymbol{K}_\varphi(\boldsymbol{\varphi} - \boldsymbol{\varphi}_d) = \boldsymbol{\kappa}^T(\boldsymbol{\varphi})\boldsymbol{\mu}_e \tag{4}$$

where $\boldsymbol{\varphi}$ is the actual orientation of end-effector; $\boldsymbol{\varphi}_d$ is the reference orientation of end-effector; $\boldsymbol{M}_\varphi$, $\boldsymbol{B}_\varphi$, and $\boldsymbol{K}_\varphi$ are the inertia diagonal matrix, the damping diagonal matrix and the stiffness diagonal matrix of the robot corresponding to the orientation, respectively. $\boldsymbol{\kappa}(\boldsymbol{\varphi})$ is the transformation matrix between the differential of the Euler angles $\dot{\boldsymbol{\varphi}}$ and angular velocities $\boldsymbol{\omega}$, and its expression is related to the Euler angles, which is

$$\boldsymbol{\omega} = \boldsymbol{\kappa}(\boldsymbol{\varphi})\dot{\boldsymbol{\varphi}} \tag{5}$$

We combine (3) and (4) to get the impedance equation of the robot:

$$\boldsymbol{M}(\ddot{\boldsymbol{x}} - \ddot{\boldsymbol{x}}_d) + \boldsymbol{B}(\dot{\boldsymbol{x}} - \dot{\boldsymbol{x}}_d) + \boldsymbol{K}(\boldsymbol{x} - \boldsymbol{x}_d) = \boldsymbol{F}_e \tag{6}$$

where $\boldsymbol{x}$, $\dot{\boldsymbol{x}}$ and $\ddot{\boldsymbol{x}}$ are actual position and orientation of the end-effector and its first and second derivatives, respectively. $\boldsymbol{x}_d, \dot{\boldsymbol{x}}_d$ and $\ddot{\boldsymbol{x}}_d$ are the reference position and orientation of the end-effector and its first and second deviations, respectively, and $\boldsymbol{x} = [\boldsymbol{p}^T, \boldsymbol{\varphi}^T]^T$. $\boldsymbol{M}$, $\boldsymbol{B}$, and $\boldsymbol{K}$ are the inertia diagonal matrix, the damping diagonal matrix and the stiffness diagonal matrix of the robot corresponding to the position and orientation, respectively. $\boldsymbol{F}_e$ is the external force and torque at the end-effector of the robot and $\boldsymbol{F}_e = [\boldsymbol{f}_e^T, (\boldsymbol{\kappa}^T(\boldsymbol{\varphi})\boldsymbol{\mu}_e)^T]^T$. Strictly speaking, parameters $\boldsymbol{M}$, $\boldsymbol{B}$, and $\boldsymbol{K}$ of robot is variant during the assembly tasks. As the variant is subtle, we assumed that these parameters have time-invariant characteristics.

If we are not considering the singularity of the robot, from (6), we can obtain the mechanical impedance $\boldsymbol{Z}$ in the frequency domain by

$$\boldsymbol{Z} = \left[\frac{\boldsymbol{F}_e}{\boldsymbol{X}(s) - \boldsymbol{X}_d(s)}\right] = \boldsymbol{M}s^2 + \boldsymbol{B}s + \boldsymbol{K} \tag{7}$$

C. MODEL OF VCS

To prevent the surface of the easily worn parts from being scratched during the assembly, this paper proposes the VCS. FIGURE 1 illustrates the concept of the VCS. We assume that the VCS is located at a distance ρ from the surface of the assembled parts. A virtual force is generated as the workpieces enter the VCS to slow its speed and complete a partial pose adjustment in order to reduce the impacts between the components that are to be assembled.

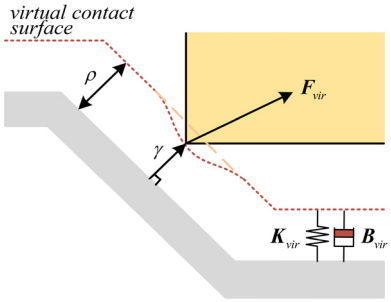

FIGURE 1. Model of a VCS.

Referring to the model of [22], this paper establishes the model of the VCS as

$$\boldsymbol{F}_{vir} = \boldsymbol{B}_{vir}\dot{\boldsymbol{x}} + \boldsymbol{K}_{vir}\boldsymbol{\Delta} \tag{8}$$

where $\boldsymbol{F}_{vir}$ is the virtual force generated by the VCS. $\boldsymbol{K}_{vir}$ and $\boldsymbol{B}_{vir}$ are the stiffness matrix and damping matrix of the VCS, respectively. $\boldsymbol{K}_{vir}$ is related to the magnitude of the virtual contact force, and $\boldsymbol{B}_{vir}$ is related to the overshoot and the peak value of the virtual contact force. After the parameter $\boldsymbol{K}_{vir}$ and $\boldsymbol{B}_{vir}$ have been determined, we can determine an appropriate value of ρ to make sure that the peg can slow its speed down before touching the real surface of the hole.

In robotics, we usually use the Jacobian matrix to relate the joint velocity to the Cartesian velocity at the end-effector as

$$\dot{\boldsymbol{x}} = \boldsymbol{J}(\boldsymbol{q})\dot{\boldsymbol{q}} \tag{9}$$

The following equation can be known from the geometric relationship of FIGURE 1.

$$\boldsymbol{\Delta} = \boldsymbol{x} - \boldsymbol{x}_{vir} = \begin{cases} \dfrac{\boldsymbol{\gamma}}{\|\boldsymbol{\gamma}\|}\rho - \boldsymbol{\gamma} & (0 < \|\boldsymbol{\gamma}\| < \rho) \\ \boldsymbol{0} & (\|\boldsymbol{\gamma}\| \geq \rho) \end{cases} \tag{10}$$

$\boldsymbol{\gamma}$ is the vertical distance from the normal of the contact surface between the two workpieces, and $\boldsymbol{x}_{vir}$ is the absolute position of the VCS.

Without the loss of generality, we reconstruct the impedance model of the robot as

$$\boldsymbol{M}(\ddot{\boldsymbol{x}} - \ddot{\boldsymbol{x}}_d) + \boldsymbol{B}(\dot{\boldsymbol{x}} - \dot{\boldsymbol{x}}_d) + \boldsymbol{K}(\boldsymbol{x} - \boldsymbol{x}_d) = \boldsymbol{\lambda}(\boldsymbol{F}_e - \boldsymbol{F}_d) \tag{11}$$

Equation (11) is consistent with the impedance (6) when $\boldsymbol{\lambda} = \boldsymbol{I}_{n\times n}$ and $\boldsymbol{F}_d = 0$.

When there is no physical contact between the workpieces to be assembled,

$$\boldsymbol{F}_e = \boldsymbol{F}_{vir} \tag{12}$$

By combining (8), (10), (11) and (12), a unified impedance model of the robot and the VCS is formed as

$$\begin{aligned} \boldsymbol{M}\ddot{\boldsymbol{x}} + (\boldsymbol{B} - \boldsymbol{\lambda}\boldsymbol{B}_{vir})\dot{\boldsymbol{x}} + (\boldsymbol{K} - \boldsymbol{\lambda}\boldsymbol{K}_{vir})\boldsymbol{x} \\ = \boldsymbol{M}\ddot{\boldsymbol{x}}_d + \boldsymbol{B}\dot{\boldsymbol{x}}_d + \boldsymbol{K}\boldsymbol{x}_d - \boldsymbol{\lambda}\boldsymbol{K}_{vir}\boldsymbol{x}_{vir} - \boldsymbol{\lambda}\boldsymbol{F}_d \end{aligned} \quad (13)$$

The system is asymptotically stable when $\boldsymbol{M}$, $\boldsymbol{B}$, and $\boldsymbol{K}$ are positive definite diagonal matrices and the stable steady-state response of the control system when $\ddot{\boldsymbol{x}}, \dot{\boldsymbol{x}}, \ddot{\boldsymbol{x}}_d$, and $\dot{\boldsymbol{x}}_d$ are zero is

$$(\boldsymbol{K} - \boldsymbol{\lambda}\boldsymbol{K}_{vir})\boldsymbol{x} = \boldsymbol{K}\boldsymbol{x}_d - \boldsymbol{\lambda}\boldsymbol{K}_{vir}\boldsymbol{x}_{vir} - \boldsymbol{\lambda}\boldsymbol{F}_d \quad (14)$$

When the system is in a steady state, it can be known from (14) that the position/orientation deviation is

$$\boldsymbol{\delta}_{pvir} = \boldsymbol{x} - \boldsymbol{x}_d = (\boldsymbol{\lambda}^{-1}\boldsymbol{K} - \boldsymbol{K}_{vir})^{-1}\left[\boldsymbol{K}_{vir}(\boldsymbol{x}_d - \boldsymbol{x}_{vir}) - \boldsymbol{F}_d\right] \quad (15)$$

The environmental model in steady state is

$$\boldsymbol{K}_{vir}(\boldsymbol{x} - \boldsymbol{x}_{vir}) = \boldsymbol{F}_{vir} \quad (16)$$

By combining (14), (15) and (16), the force/torque deviation is gained as

$$\boldsymbol{\delta}_{fvir} = \boldsymbol{F}_e - \boldsymbol{F}_d = \boldsymbol{\lambda}^{-1}\boldsymbol{K}\boldsymbol{\delta}_{pvir} \quad (17)$$

In general, when it is in a steady state, $\boldsymbol{K}$ is much larger than $\boldsymbol{\lambda}$ and $\boldsymbol{K}_{vir}$, and so the position/orientation deviation and the force/torque deviation in the steady state are very small and can be ignored. Thus, the impedance model of the robot during the assembly process can be obtained.

Inertia, damping, and stiffness need to be appropriately selected according to different work tasks. For more rigid component assembly tasks, we generally choose a smaller ambient stiffness and proper damping. The role of the inertia mainly ensures that the workpieces that are to be assembled are gently contacted.

Successful assembly tasks depend on the desired trajectory and impedance parameters that are selected in conjunction with the particular operation. However, in order to achieve the smooth operation of the robot, we also need to know the external force/torque of the end-effector during the assembly. In the next section, we will discuss how to obtain the contact force/torque between the robot end-effector and the external environment.

III. CALCULATION OF EXTERNAL FORCE/TORQUE

Many scholars calculate the external force/torque at the end-effector of the robot by establishing an external torque observer. However, we found that the external torque observer cannot accurately calculate the external force/torque after testing. Therefore, the identification of the robot dynamic model is used to determine the external torque of the robot joints in this paper.

A. IDENTIFICATION OF ROBOT DYNAMIC MODEL

In this paper, the external torque of each joint is determined by the subtraction of the torque value that is read from the driver and the torque value that is calculated according to identification results. First, the dynamic model of the robot needs to be identified. To simplify the process of dynamic parameters identification, we assumed that the friction is a simple nonlinear static function of the velocity, this assumptions can be considered valid when the robot runs in low speed with light loads [23], and the friction model of the robot joints is chosen as

$$\boldsymbol{F}_{f1}(\boldsymbol{q}, \dot{\boldsymbol{q}}) = \boldsymbol{\mu}_{\boldsymbol{c}}\ \mathrm{sgn}\ (\dot{\boldsymbol{q}}) + \boldsymbol{\mu}_{\boldsymbol{v}}\dot{\boldsymbol{q}} \quad (18)$$

The robot dynamic model that needs to be identified is

$$\boldsymbol{M}(\boldsymbol{q})\ddot{\boldsymbol{q}} + \boldsymbol{C}(\boldsymbol{q}, \dot{\boldsymbol{q}})\dot{\boldsymbol{q}} + \boldsymbol{G}(\boldsymbol{q}) + \boldsymbol{\mu}_{\boldsymbol{c}}\ \mathrm{sgn}\ (\dot{\boldsymbol{q}}) + \boldsymbol{\mu}_{\boldsymbol{v}}\dot{\boldsymbol{q}} = \boldsymbol{\tau}_d \quad (19)$$

Equation (19) is rewritten into a linear form using the centroid parameters or Newton-Euler parameters:

$$\boldsymbol{\tau}_d = \boldsymbol{\Phi}(\boldsymbol{q}, \dot{\boldsymbol{q}}, \ddot{\boldsymbol{q}})\boldsymbol{\theta} \quad (20)$$

where $\boldsymbol{\Phi} \in \boldsymbol{R}^{n\times 12n}$ is the Jacobian matrix corresponding to τ_d and, as a regression matrix for identifying $\boldsymbol{\theta}$, it is only related to the DH parameters of the robot and the displacement, velocity and acceleration of the joints. $\boldsymbol{\theta} \in \boldsymbol{R}^{12n}$ is the dynamic parameter set that needs to be identified and it is composed of $n \times \theta_i \in \boldsymbol{R}^{12}$, where

$$\boldsymbol{\theta}_i = [I_{xxi}, I_{yyi}, I_{zzi}, I_{xyi}, I_{xzi}, I_{yzi}, m_i r_{xi}, m_i r_{yi}, m_i r_{zi}, m_i, \mu_{ci}, \mu_{vi}]^T.$$

It contains the inertial tensor, the first-order mass moment and the friction coefficient. The specific expression can be found in the literature [24], where n is the total number of equivalent links of the robot that need to be identified.

Some dynamic parameters have no effect on joint torque, and thus the regression matrix $\boldsymbol{\Phi} \in \boldsymbol{R}^{n\times 12n}$ is not full rank. Therefore, equation (20) needs to be fully ranked through recombination. To simplify the identification process, the 1/2/3 joints and the 1/4/5/6 joints of the robot are divided into two groups, respectively, and each group is designed with two excitation trajectories. The excitation trajectory $q_i(t)$ is based on the fifth-order Fourier series, it is

$$q_i(t) = a_i + \sum_{k=1}^{z} b_{ik}\sin(kwt) + \sum_{k=1}^{z} c_{ik}\cos(kwt) \quad (21)$$

where a_i is the starting point of the joint excitation trajectory, b_{ik} and c_{ik} are the coefficients of the fitted trajectory.

The parameters of the excitation trajectory are determined by the construction and optimization of the objective function. In this paper, the specific optimization objective function is

$$\begin{cases} \min cond(\boldsymbol{\Phi}) \\ \boldsymbol{q}_{i\min} \le \boldsymbol{q}_i(t) \le \boldsymbol{q}_{i\max} \\ \dot{\boldsymbol{q}}_{i\min} \le \dot{\boldsymbol{q}}_i(t) \le \dot{\boldsymbol{q}}_{i\max} \\ \ddot{\boldsymbol{q}}_{i\min} \le \ddot{\boldsymbol{q}}_i(t) \le \ddot{\boldsymbol{q}}_{i\max} \\ WS(\boldsymbol{q}_i(t)) \subset WS_{act} \\ \boldsymbol{q}(0) = \dot{\boldsymbol{q}}(0) = \ddot{\boldsymbol{q}}(0) = \boldsymbol{0} \end{cases} \quad (22)$$

where $\boldsymbol{q}_{i\min}$, $\boldsymbol{q}_{i\max}$, $\dot{\boldsymbol{q}}_{i\min}$, $\dot{\boldsymbol{q}}_{i\max}$, $\ddot{\boldsymbol{q}}_{i\min}$ and $\ddot{\boldsymbol{q}}_{i\max}$ are the minimum and maximum limits of the joint angle,

angular velocity and angular acceleration of the i th joint, respectively; $WS(\boldsymbol{q}_i(t))$ and WS_{act} represent the actual workspace constraint of each joint and the end effector. $\boldsymbol{q}(0) = \dot{\boldsymbol{q}}(0) = \ddot{\boldsymbol{q}}(0) = \boldsymbol{0}$ ensures a smooth start of the track without jitter; and $cond(\boldsymbol{\Phi})$ is the condition number of the nonsingular matrix $\boldsymbol{\Phi}$. Considering the complexity and iterative speed of optimization, a genetic algorithm (GA) is employed to perform the iterative calculation.

In this paper, the kinetic parameters are solved by the weighted least squares method considering the influence of the joint torque noise. The weight is the inverse equation of the torque noise covariance. The weighted least squares estimation of the inertia parameters is

$$\hat{\boldsymbol{\theta}}_{dyn} = (\boldsymbol{\Phi}_{Ndyn}^T \boldsymbol{\Sigma}^{-1} \boldsymbol{\Phi}_{Ndyn})^{-1} \boldsymbol{\Phi}_{Ndyn}^T \boldsymbol{\Sigma}^{-1} \boldsymbol{\tau}_N \tag{23}$$

$\boldsymbol{\tau}_N$ is the joint torque collected from the driver when the robot is running the excitation trajectory, $\boldsymbol{\Phi}_{Ndyn} \in \boldsymbol{R}^{n\times 12n}$ is the Jacobian matrix corresponding to $\boldsymbol{\tau}_N$, and N is the number of sets of joint torques that are collected from the driver.

The friction model of robot joints used in (18) is linear and can hardly express the true friction. To this end, this paper proposes a secondary compensation for the identification of the dynamic model.

Due to the special transmission structure of the harmonic reducer, the friction is related not only to the rotational speed but also to the rotational angle at low speed. The compensation algorithm here is divided into two parts. The friction torque term that is related to the angular displacement adopts the second-order Fourier series, and the friction torque term related to the angular velocity adopts the third-order polynomial function, as shown in (24):

$$\begin{aligned}\boldsymbol{F}_{f2}(\boldsymbol{q}, \dot{\boldsymbol{q}}) = \boldsymbol{k}_1 \sin \boldsymbol{q} + \boldsymbol{k}_2 \cos \boldsymbol{q} + \boldsymbol{k}_3 \sin(2\boldsymbol{q}) \\ + \boldsymbol{k}_4 \cos(2\boldsymbol{q}) + \boldsymbol{a}\dot{\boldsymbol{q}}^3 + \boldsymbol{b}\dot{\boldsymbol{q}}^2 + \boldsymbol{c}\dot{\boldsymbol{q}} + \boldsymbol{d}\end{aligned} \tag{24}$$

where $\boldsymbol{k}_1$, $\boldsymbol{k}_2$, $\boldsymbol{k}_3$, $\boldsymbol{k}_4$, $\boldsymbol{a}$, $\boldsymbol{b}$, $\boldsymbol{c}$, and $\boldsymbol{d}$ are the parameters to be identified. $\boldsymbol{F}_{f2}(\boldsymbol{q}, \dot{\boldsymbol{q}})$ is the friction torque related to displacement and velocity of joints.

The identification method of the robot dynamic model is implemented on a 6-DOF collaborative robot that was developed by the laboratory, and its structure is shown in FIGURE 2.

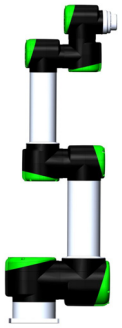

FIGURE 2. Laboratory-developed robots.

Taking joint 2 with the largest maximum torque error as an example, we design an appropriate verification trajectory to verify the accuracy of the identified dynamic model. FIGURE 3 is a comparison of the torque that is acquired from the driver and the torque that is calculated by the identified model of joint 2.

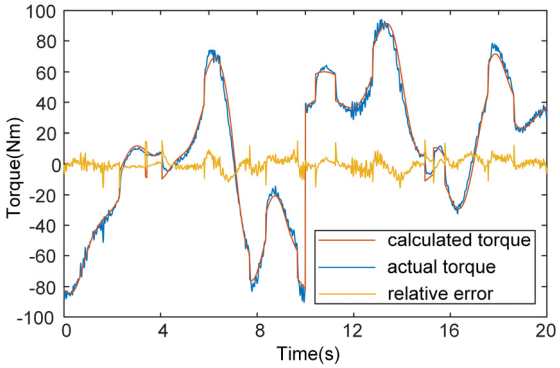

FIGURE 3. Dynamic model verification of joint 2.

FIGURE 4 shows the error comparison of the identified model before and after the secondary compensation. It can be seen that the torque error after the secondary compensation is reduced by approximately 50%.

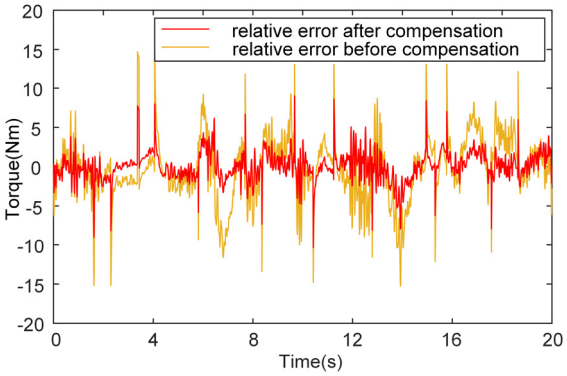

FIGURE 4. Error comparison of joint 2 before and after compensation.

The accuracy of the identification result is evaluated by the root mean square error (RMSE) indicator, as shown in (25).

$$\mathrm{RMSE} = \sqrt{\frac{\sum_{i=1}^{n} (X_{i,calc} - X_{i,act})}{n}} \tag{25}$$

where n is the number of the sets of data,$X_{i,calc}$, $X_{i,act}$ is the calculated and actual value of the ith point.

After calculation, the root-mean-square error of the identification of joints 1, 2 and 3 joints is 1.8365 Nm, and the root-mean-square error of the identification of joints 4, 5 and 6 joints is 0.3654 Nm. The relative error of the identification for joints 1, 2 and 3 joints and joints 4, 5 and 6 are under 5%.

B. EXTERNAL CARTESIAN FORCE/TORQUE CALCULATION

The Jacobian matrix $\boldsymbol{J}(\boldsymbol{q})$ relates the joint velocity to the end Cartesian velocity, while $\boldsymbol{J}^{\dagger}(\boldsymbol{q})$ maps the joint moment to the end force/torque. The Jacobian matrix of the robot's end joint relative to the base coordinate system is

$$\boldsymbol{J}(\boldsymbol{q})=\begin{bmatrix}\boldsymbol{Z}_1\times{}^1\boldsymbol{P}_n^0 & \boldsymbol{Z}_2\times{}^2\boldsymbol{P}_n^0 & \ldots & \boldsymbol{Z}_i\times{}^i\boldsymbol{P}_n^0 & \ldots & \boldsymbol{Z}_n\times{}^n\boldsymbol{P}_n^0\\ \boldsymbol{Z}_1 & \boldsymbol{Z}_2 & \ldots & \boldsymbol{Z}_i & \ldots & \boldsymbol{Z}_n\end{bmatrix} \tag{26}$$

where $\boldsymbol{i}=1\ldots n$, $\boldsymbol{Z}_i$ is the unit vector of the z_i-axis of the ith joint coordinate system, ${}^i\boldsymbol{P}_n^0$ is the representation of the position of the end coordinate system origin relative to the joint coordinate system $\{o_i-x_iy_iz_i\}$ in the base coordinate system $\{o-xyz\}$, and n is the number of degrees of freedom for the robot. The Jacobian matrix can only be computed for a point in the system, the external force/torque calculating method can only estimate force/torque at the tip of the end-effector. So we assumed that contact occurs only between the tip of the end-effector and the workspieces.

Note that the joint torque that is collected by the driver is $\boldsymbol{\tau}_c \in \boldsymbol{R}^n$, it is the filtered joint torque when the robot is executing a task and it contains the original driving torque and external torque, like a joint torque sensor value. The joint torque that is calculated by the identified dynamic model is $\boldsymbol{\tau}_{iden} \in \boldsymbol{R}^n$, and the external force/torque at the end-effector is

$$\boldsymbol{F}_{car}=(\boldsymbol{J}^T(\boldsymbol{q}))^{\dagger}(\boldsymbol{\tau}_c-\boldsymbol{\tau}_{iden}) \tag{27}$$

The joint torque that is collected by the driver has a lot of noise. For this reason, the collected torque is filtered using the Kalman filter, which is convenient for computer programming and can update and process the data that are collected in the field in real time.

The Kalman gain of the joint torque value at time k is

$$K(k)=P(k|k-1)/(P(k|k-1)+R) \tag{28}$$

The filtered torque value is

$$x(k|k)=x(k-1|k-1)+K(k)\cdot(z(k)-x(k-1|k-1)) \tag{29}$$

where $z(k)$ is the torque value collected at time k.

The error covariance of the torque value is

$$P(k+1|k)=(1-K(k))\cdot P(k|k-1)+Q \tag{30}$$

Among them, Q and R are given artificially and tested through many experiments. Their physical meaning is the covariance of the noise signal. The initial values of x and P can be arbitrarily given, and the powerful Kalman filter can immediately eliminate an unreasonable value, but P cannot be zero. $x(k|k)$ is the filtered value that we want, $x(k|k)$ and $P(k|k)$ will be used as $x(k-1|k-1)$ and $P(k-1|k-1)$, respectively, in the iteration of the next moment. The filtering effect is shown in FIGURE 5.

In order to verify the accuracy of the external force/torque calculation algorithm, we installed a 6-dimensional force/torque sensor at the end-effector of the robot. As an example, the calculated force $\boldsymbol{F}_z$ in the z-axis direction is compared with a value collected by sensor, as shown in FIGURE 6.

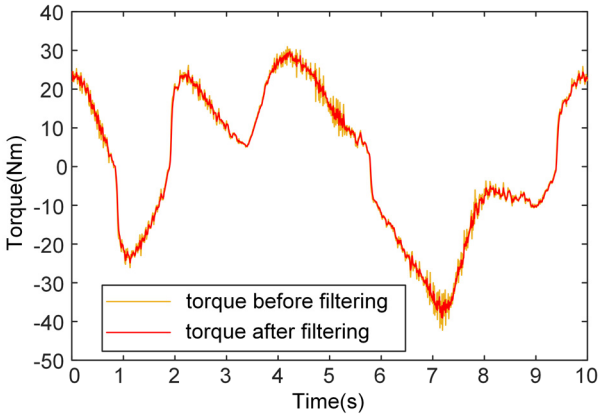

FIGURE 5. Joint torque after filtering by the Kalman filter.

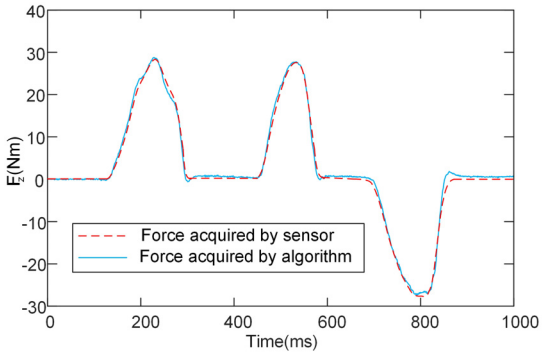

FIGURE 6. Calculated value and sensor value of force in the z-axis direxion.

IV. ASSEMBLY STRATEGY

After we studied and analyzed the artificial assembly, we found that humans do not need to follow accurate trajectories or apply accurate forces when assembling, but they rely heavily on human flexibility. To this end, we propose a kind of human-like compliant control algorithm.

In the assembly process, it is necessary not only to make the robot flexible but also to make the end-effector of the robot have higher motion precision. However, the impedance control does not actually control the position and orientation of the robotic arm. To control the position and orientation of the robot, we usually use the position control as the inner loop and the impedance control as the outer loop. Industrial robots typically use position control based on simple PID control because it is easier to meet the point-to-point accuracy requirements. If the information acquisition frequency of the inner loop of the position control is faster than the information acquisition frequency of the outer loop of the impedance control, the inner loop of the position can better resist the external interference than the inner loop of the force [25], [26]. Therefore, in this paper, the position control based on the proportion-derivative (PD) control is used as the control inner loop.

The flexibility of the assembly process is considered first. The driving torque of the joint motor that is obtained

by (1) and (2) is

$$\boldsymbol{\tau}_d = \boldsymbol{M}(\boldsymbol{q})\ddot{\boldsymbol{q}} + \boldsymbol{C}(\boldsymbol{q}, \dot{\boldsymbol{q}})\dot{\boldsymbol{q}} + \boldsymbol{G}(\boldsymbol{q}) + \boldsymbol{F}_f(\boldsymbol{q}, \dot{\boldsymbol{q}}) + \boldsymbol{J}^T(\boldsymbol{q})\boldsymbol{F}_e \quad (31)$$

The derivative of (9) is obtained as

$$\ddot{\boldsymbol{x}} = \boldsymbol{J}(\boldsymbol{q})\ddot{\boldsymbol{q}} + \dot{\boldsymbol{J}}(\boldsymbol{q})\dot{\boldsymbol{q}} \quad (32)$$

Further, we can get

$$\ddot{\boldsymbol{q}} = \boldsymbol{J}^{\dagger}(\boldsymbol{q})[\ddot{\boldsymbol{x}} - \dot{\boldsymbol{J}}(\boldsymbol{q})\dot{\boldsymbol{q}}] \quad (33)$$

where $\boldsymbol{J}^{\dagger}(\boldsymbol{q})$ is the generalized inverse of $\boldsymbol{J}(\boldsymbol{q})$ and $\boldsymbol{J}^{\dagger}(\boldsymbol{q}) = \boldsymbol{J}^T(\boldsymbol{q})[\boldsymbol{J}(\boldsymbol{q})\boldsymbol{J}^T(\boldsymbol{q})]^{-1}$.

If the singularity of the robot is not considered, that is, $\boldsymbol{J}(\boldsymbol{q})$ is a square matrix, then

$$\boldsymbol{J}^{\dagger}(\boldsymbol{q}) = \boldsymbol{J}^{-1}(\boldsymbol{q}) \quad (34)$$

$$\ddot{\boldsymbol{q}} = \boldsymbol{J}^{-1}(\boldsymbol{q})[\ddot{\boldsymbol{x}} - \dot{\boldsymbol{J}}(\boldsymbol{q})\dot{\boldsymbol{q}}] \quad (35)$$

Before performing the assembly task, you can simulate the motion trajectory of the end-effector in order to ensure that there is no singular situation during the movement. Therefore, the singularity of the robot can be ignored when designing the control law. Substituting (34) into (30) yields

$$\boldsymbol{\tau}_d = \boldsymbol{M}(\boldsymbol{q})\boldsymbol{J}^{-1}(\boldsymbol{q})[\ddot{\boldsymbol{x}} - \dot{\boldsymbol{J}}(\boldsymbol{q})\dot{\boldsymbol{q}}] + \boldsymbol{C}(\boldsymbol{q}, \dot{\boldsymbol{q}})\dot{\boldsymbol{q}} + \boldsymbol{G}(\boldsymbol{q}) + \boldsymbol{F}_f(\boldsymbol{q}, \dot{\boldsymbol{q}}) + \boldsymbol{J}^T(\boldsymbol{q})\boldsymbol{F}_e \quad (36)$$

where $\boldsymbol{x} = [\boldsymbol{p}^T, \boldsymbol{\varphi}^T]^T$.

Performing a Lagrangian transformation on (33) yields an impedance acceleration adjustment of

$$\Delta\ddot{\boldsymbol{x}} = \ddot{\boldsymbol{X}}(s) - \ddot{\boldsymbol{X}}_d(s) = \frac{s^2(\boldsymbol{F}_e - \boldsymbol{F}_d)}{\boldsymbol{M}s^2 + \boldsymbol{B}s + \boldsymbol{K}} \quad (37)$$

Therefore, the impedance velocity and displacement adjustment can be obtained as

$$\Delta\dot{\boldsymbol{x}} = \dot{\boldsymbol{X}}(s) - \dot{\boldsymbol{X}}_d(s) = \frac{s(\boldsymbol{F}_e - \boldsymbol{F}_d)}{\boldsymbol{M}s^2 + \boldsymbol{B}s + \boldsymbol{K}} \quad (38)$$

$$\Delta\boldsymbol{x} = \boldsymbol{X}(s) - \boldsymbol{X}_d(s) = \frac{(\boldsymbol{F}_e - \boldsymbol{F}_d)}{\boldsymbol{M}s^2 + \boldsymbol{B}s + \boldsymbol{K}} \quad (39)$$

Note that the input displacement of the inner position loop is $\boldsymbol{x}_c$ and $\boldsymbol{x}_c = [\boldsymbol{p}_c^T, \boldsymbol{\varphi}_c^T]^T$. Then,

$$\boldsymbol{x}_c = \boldsymbol{x}_d - \Delta\boldsymbol{x} \quad (40)$$

$$\dot{\boldsymbol{x}}_c = \dot{\boldsymbol{x}}_d - \Delta\dot{\boldsymbol{x}} \quad (41)$$

$$\ddot{\boldsymbol{x}}_c = \ddot{\boldsymbol{x}}_d - \Delta\ddot{\boldsymbol{x}} \quad (42)$$

The actual position of the end-effector in the Cartesian space is $\boldsymbol{x}_m = [\boldsymbol{p}_m^T, \boldsymbol{\varphi}_m^T]^T$, and the position control is implemented by setting a new input variable $\boldsymbol{a}_m$. Therefore, so we can rewrite (35) as

$$\boldsymbol{\tau}_d = \boldsymbol{M}(\boldsymbol{q})\boldsymbol{J}^{-1}(\boldsymbol{q})[\boldsymbol{a}_m - \dot{\boldsymbol{J}}(\boldsymbol{q})\dot{\boldsymbol{q}}] + \boldsymbol{C}(\boldsymbol{q}, \dot{\boldsymbol{q}})\dot{\boldsymbol{q}} + \boldsymbol{G}(\boldsymbol{q}) + \boldsymbol{F}_f(\boldsymbol{q}, \dot{\boldsymbol{q}}) + \boldsymbol{J}^T(\boldsymbol{q})\boldsymbol{F}_e \quad (43)$$

where $\boldsymbol{a}_m = [\boldsymbol{a}_\upsilon^T, \boldsymbol{a}_\omega^T]^T$, and $\boldsymbol{a}_\upsilon$ and $\boldsymbol{a}_\omega$ are the accelerations that corresponds to the position and the orientation, respectively. According to (3), the following is proposed:

$$\boldsymbol{a}_\upsilon = \ddot{\boldsymbol{p}}_c + \boldsymbol{K}_{d\upsilon}(\dot{\boldsymbol{p}}_c - \dot{\boldsymbol{p}}_m) + \boldsymbol{K}_{p\upsilon}(\boldsymbol{p}_c - \boldsymbol{p}_m) \quad (44)$$

where $\boldsymbol{K}_{d\upsilon}$ and $\boldsymbol{K}_{p\upsilon}$ are the gain coefficients of the position part in the inner loop.

According to (4), the following is proposed:

$$\boldsymbol{a}_\omega = \boldsymbol{\kappa}(\boldsymbol{\varphi}_m)[\ddot{\boldsymbol{\varphi}}_c + \boldsymbol{K}_{d\omega}(\dot{\boldsymbol{\varphi}}_c - \dot{\boldsymbol{\varphi}}_m) + \boldsymbol{K}_{p\omega}(\boldsymbol{\varphi}_c - \boldsymbol{\varphi}_m)] + \dot{\boldsymbol{\kappa}}(\boldsymbol{\varphi}_m)\dot{\boldsymbol{\varphi}}_m \quad (45)$$

where $\boldsymbol{K}_{d\omega}$ and $\boldsymbol{K}_{p\omega}$ are the gain coefficients of the orientation part in the inner loop.

To simplify (43), let

$$\boldsymbol{u} = \boldsymbol{J}^{-1}(\boldsymbol{q})[\boldsymbol{a}_m - \dot{\boldsymbol{J}}(\boldsymbol{q})\dot{\boldsymbol{q}}] = \boldsymbol{J}^{-1}(\boldsymbol{q})\left(\begin{bmatrix} \ddot{\boldsymbol{p}}_c + \boldsymbol{K}_{d\upsilon}(\dot{\boldsymbol{p}}_c - \dot{\boldsymbol{p}}_m) + \boldsymbol{K}_{p\upsilon}(\boldsymbol{p}_c - \boldsymbol{p}_m) \\ \boldsymbol{\kappa}(\boldsymbol{\varphi}_m)[\ddot{\boldsymbol{\varphi}}_c + \boldsymbol{K}_{d\omega}(\dot{\boldsymbol{\varphi}}_c - \dot{\boldsymbol{\varphi}}_m) + \boldsymbol{K}_{p\omega}(\boldsymbol{\varphi}_c - \boldsymbol{\varphi}_m)] + \dot{\boldsymbol{\kappa}}(\boldsymbol{\varphi}_m)\dot{\boldsymbol{\varphi}}_m \end{bmatrix} - \dot{\boldsymbol{J}}(\boldsymbol{q})\dot{\boldsymbol{q}}\right) \quad (46)$$

The control law is designed as

$$\boldsymbol{\tau}_d = \boldsymbol{M}(\boldsymbol{q})\boldsymbol{u} + \boldsymbol{C}(\boldsymbol{q}, \dot{\boldsymbol{q}})\dot{\boldsymbol{q}} + \boldsymbol{G}(\boldsymbol{q}) + \boldsymbol{F}_f(\boldsymbol{q}, \dot{\boldsymbol{q}}) + \boldsymbol{J}^T(\boldsymbol{q})\boldsymbol{F}_e \quad (47)$$

Note that $\boldsymbol{K}_d = [\boldsymbol{K}_{d\upsilon}^T, \boldsymbol{K}_{d\omega}^T]^T$, $\boldsymbol{K}_p = [\boldsymbol{K}_{p\upsilon}^T, \boldsymbol{K}_{p\omega}^T]^T$, and the whole control flow chart is shown in FIGURE 7. The flow chart consists of two parts: one is the inner loop of position control and the other is the outer loop of impedance control. The displacement, velocity and acceleration information of the motor that are read from the driver cannot be directly used, and thus a state observer is constructed for this purpose. The state observer can calculate the displacement, velocity, and acceleration of each joint and perform Kalman filtering which has been illustrated in section III-B on the acquired joints' torque value. The input of coordinate transformation is the Cartesian position, velocity and acceleration of the robot end-effector and its output is the angular position, velocity and acceleration of each robot joint. Based on the constructed external torque observer in section III, the external force/torque of the Cartesian space during the assembly process can be obtained. The external force/torque is used as the input of the impedance control, and the compensation displacement, velocity and acceleration of each joint are written according to the impedance model in order to realize the compliance control of the robot.

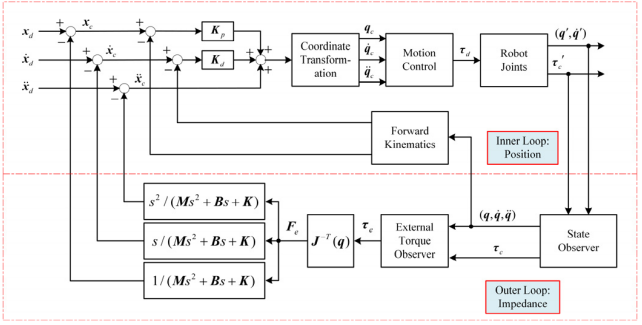

FIGURE 7. The flow chart of compliant control.

This article takes the peg-in-hole assembly as an example to illustrate the specific assembly strategy. In this paper,

the hole is fixed on the workbench, and the peg is clamped by the robot's end-effector. After the robot's end-effector moves the peg above the hole, it sends an instruction to the robot to run vertically to the hole. The peg corner contacts the VCS at first, taking the yz plane as an example, as shown in FIGURE 8. There are three possibilities for the peg to contact the VCS, and the peg can complete the deceleration and a portion of the orientation transition after contacting the VCS. The position of peg and hole are known in advance. For parameter α, it can be calculated by the orientation angle of the peg. For parameter β, it's the chamfer of the hole and can be known in advance. For parameter a, it can be calculated as

$$a = (l - L)/\cos\alpha \tag{48}$$

where l and L are the position of point A and point C in the z-axis direction.

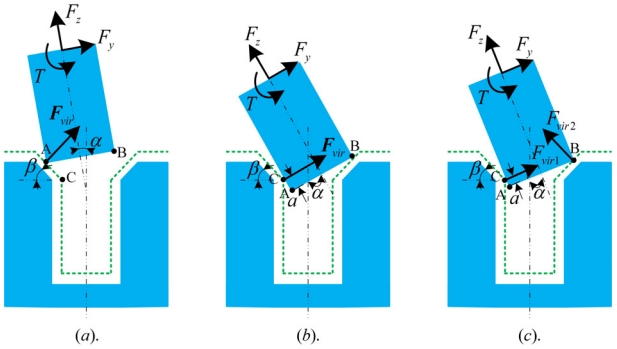

FIGURE 8. Contact between the peg and the VCS.

The position of point A and B related to base coordinate are calculated in real time, and the position of VCS is known. Thus we can judge when and how the peg reaches the VCS by determining where point A and point B are.

From the geometric relationship in FIGURE 8(a), we can get

$$\begin{cases} F_y = F_{vir}\sin(\alpha+\beta) \\ F_z = F_{vir}\cos(\alpha+\beta) \\ T_x = F_y L - F_z r \end{cases} \tag{49}$$

The value of F_{vir} is obtained by (8), where F_y and F_z are the force received by the end joint in the y-axis direction and the x-axis direction, respectively, and T_x is the torque in the x-axis direction.α and β are as shown in FIGURE 8. We set the position adjustment of the end-effector along the y-axis and z-axis as $\Delta\xi_y$ and $\Delta\xi_z$, respectively, and the orientation adjustment is $\Delta\psi$. Then,

$$\begin{cases} \Delta\xi_y = \dfrac{F_{vir}\sin(\alpha+\beta)}{M_y s^2 + B_y s + K_y} \\ \Delta\xi_z = \dfrac{F_{vir}\cos(\alpha+\beta)}{M_z s^2 + B_z s + K_z} \\ \Delta\psi = \dfrac{F_{vir}L\sin(\alpha+\beta) - F_{vir} r\cos(\alpha+\beta)}{M_{tx} s^2 + B_{tx} s + K_{tx}} \end{cases} \tag{50}$$

M_y, B_y, and K_y are the impedance parameters of the robot corresponding to the force in the y-axis direction; M_z, B_z, and K_z are the impedance parameters of the robot corresponding to the force in the z-axis direction; and M_{tx}, B_{tx}, and K_{tx} are the impedance parameters of the robot corresponding to the torque in the x-axis direction.

The position adjustment and orientation adjustment in FIGURE 8(b) and FIGURE 8(c) can be obtained similarly. For FIGURE 8(b), we can get

$$\begin{cases} \Delta\xi_y = \dfrac{F_{vir}}{M_y s^2 + B_y s + K_y} \\ \Delta\xi_z = 0 \\ \Delta\psi = \dfrac{F_{vir}(L-a)}{M_{tx} s^2 + B_{tx} s + K_{tx}} \end{cases} \tag{51}$$

For FIGURE 8(c), we can get

$$\begin{cases} \Delta\xi_y = \dfrac{F_{vir1} - F_{vir2}\cos(\alpha+\beta)}{M_y s^2 + B_y s + K_y} \\ \Delta\xi_z = \dfrac{F_{vir2}\sin(\alpha+\beta)}{M_z s^2 + B_z s + K_z} \\ \Delta\psi = \dfrac{(F_{vir1} - F_{vir2})(L-a)\cos(\alpha+\beta) + F_{vir2} r\sin(\alpha+\beta))}{M_{tx} s^2 + B_{tx} s + K_{tx}} \end{cases} \tag{52}$$

After the peg contacts the VCS in order to complete the deceleration and partial orientation adjustment, it will contact the real surface of the hole. A real force/torque will be detected at the end-effector of the robot. FIGURE 9 shows four cases of contact between peg and real hole. In real contact, the robot can adjust itself to let peg into hole by sensing the contact force/torque between peg and hole.

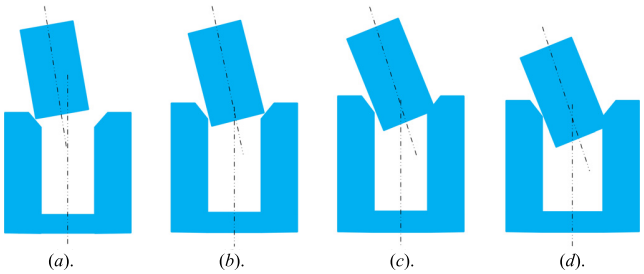

FIGURE 9. Contact between the peg and the real hole.

V. EXPERIMENT

To verify the proposed flexible algorithm and assembly strategy, the 6-DOF collaborative robot that was developed by the laboratory was used to complete the peg-in-hole assembly experiment, and the coordinate system $o_w - x_w y_w z_w$ of the peg is shown in FIGURE 10.

According to the system integration and the characteristics of fieldbus, TwinCAT soft PLC is selected as the central control unit and it is responsible for the control signal transmission and measurement data acquisition. Beckhoff TwinCAT software is a real-time control software based on the Windows software and hardware platform [27].

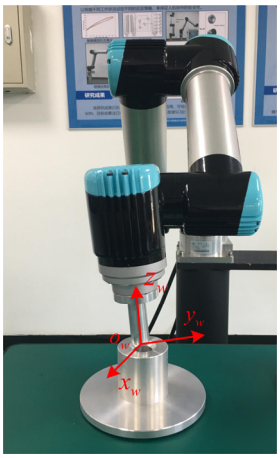

FIGURE 10. The coordinate system of the end-effector.

The real-time feature can guarantee that the input, calculation and output of signals are completed in a very short time, and processed in time according to the changes of working conditions. It enables the real-time control of I/O modules and drives the internal changes to the underlying Windows. The driver communicates with TwinCAT via EtherCAT, and TwinCAT uses ADS communication to interact with the HMI written by LabVIEW. The real-time task can be set in TwinCAT and the system latency is monitored during the whole process.

We combine the qualitative analysis with the multiple experiments and finally select ρ, K_{vir} and B_{vir} as 3mm, 6000 N/m and 40 Ns/m in the z-axis direction. And the impedance parameters are chosen as

$$\begin{aligned} \boldsymbol{M} &= diag[2, 2, 2, 1, 1, 1]\text{Kg} \\ \boldsymbol{B} &= diag[40, 40, 40, 40, 40, 40]\text{Nsm}^{-1} \\ \boldsymbol{K} &= diag[1000, 1000, 5000, 2000, 2000, 2000]\text{N/m} \end{aligned} \quad (53)$$

The peg is directly connected to the end flange of the robot by screws. The diameter of the peg is 21.5 mm and the length is 60 mm. The base of the hole piece is fixed on the workbench with glue. The diameter of the hole is 22 mm, and the edge of the hole has a chamfer of 5 mm$\times$45°. The peg-in-hole assembly is roughly divided into four steps: the approaching step, the virtual contact step, the physical contact step, and the insertion step. Since the end-effector in the z-axis direction needs to overcome large resistance during the insertion process, a force margin is reserved in the z-axis direction. During the peg-in-hole task, the robot is tracking a desired trajectory. The first part of the trajectory is followed by the robot without interacting with the environment. During the second, third and fourth part, the robot interacts with the VCS and the workspieces, and is forced to follow a new trajectory by regulating the contact forces in order to obtain a suitable tracking. When the peg is dragged over the hole, the robot is instructed to bring the peg close to the hole. The peg first contacts the VCS to complete the deceleration and a part of the posture adjustment. After that, the peg will contact the real surface of the hole to further adjust the orientation of the peg so that the peg can be smoothly inserted into the hole.

FIGURE 11 shows force/torque and position change of the peg when completing a flexible assembly task. Also, the Cartesian force/torque calculated by the algorithm is compared with the value collected by sensor (AEF-6A250-Tyoe-S-ET). It can be seen from the figure that the accuracy of external force/torque calculation algorithm is satisfied. Since the peg is dragged over the hole, both the position and orientation error exist, and the VCS was selected as 3 mm from the surface of the hole. For step I, the peg approaches the hole. At the end of the first stage, the peg corner contacts the VCS. In the step II, the peg interacts with the VCS. Through the positional slope of the z-axis in this stage, it can be seen that the peg obviously decelerates its velocity. Then the VCS can reduce the impact between them. The force in the z-axis direction is shown as an example to illustrate the effectiveness of the VCS. As shown in FIGURE 12,

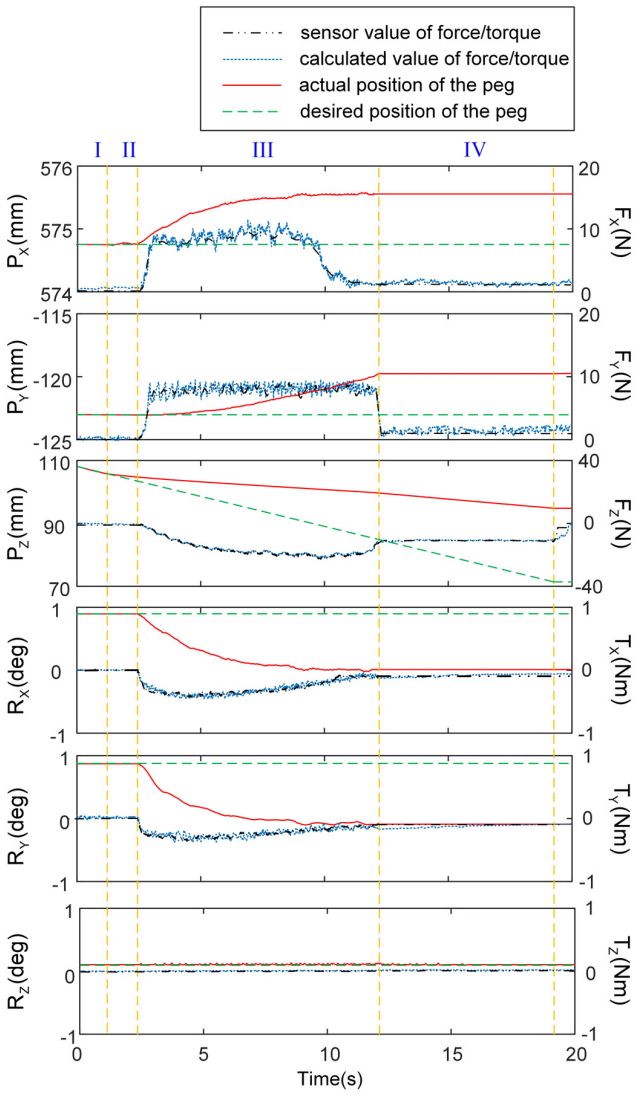

FIGURE 11. Force/torque and position change of the peg.

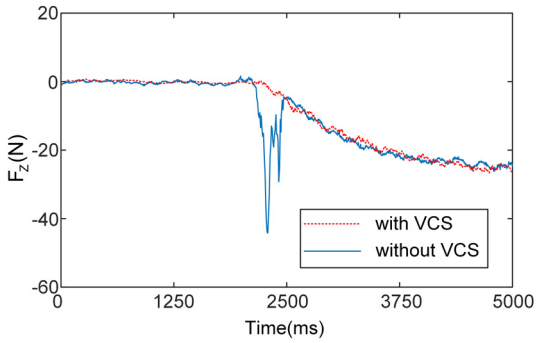

FIGURE 12. Comparison of contact force in z-axis direction with and without VCS.

the contact is smooth when the VCS assembly optimization method is applied. If this optimization method is excluded, it's obvious that the contact between of peg and real hole has a huge impact. Thus the VCS in this paper can reduce wear and damage of workpieces. The step III is the real contact stage between the peg and the hole and the force/torque are growing rapidly. The peg is further adjusted in order to insert the peg into the hole. Since the real contact force is generated at this stage, the impedance control starts to take effect. The adjustment of position is most frequent in this phase. It can be seen from the figure that the fluctuation range of the force does not exceed 4N. In the step IV, the force/torque decrease quickly and remain stable while the peg is moving downward along the inner wall of the hole, the frictional resistance is overcome by the force margin in the z-axis direction. In addition, the positional adjustment is almost zero at this stage, thus indicating that the insertion process is smooth. At the end of step IV, the motion of the robot is stopped. It can be seen from the force/torque variation in the figure that the peg can achieve environmental adaptability along the chamfer and the whole process is stable.

FIGURE 13 shows the trajectory of the origin of the end coordinate system in 3-dimensional (3D) space during the insertion. It can be seen from the figure that the trajectory is smooth and the peg-in-hole process is stable.

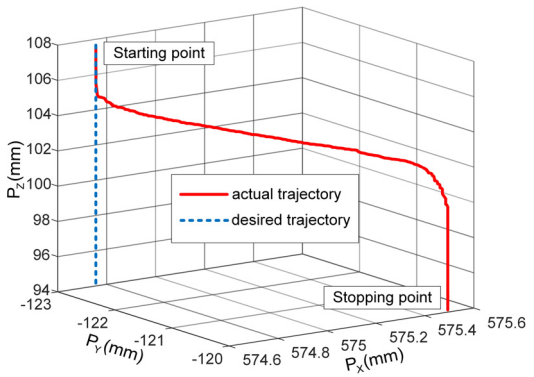

FIGURE 13. The 3D trajectory of the end-effector.

VI. CONCLUSION

This paper proposes an active compliant control method that ensures the flexibility of the robot to the external environment without the need to install an external force/torque sensor. A unified impedance model of the robot and the environment is established. Based on the model, the VCS is proposed, and the force and position deviations that are caused by the existence of the VCS are analyzed. Experiments have shown that the existence of a VCS allows the peg to slow down and complete a partial position/orientation adjustment before contacting the real surface of the hole and decreasing the range that has to be adjusted during real contact. In this paper, the robot dynamic model is identified. To improve the identification accuracy, a new friction compensation model is proposed for secondary compensation. After the secondary compensation, the dynamic model's accuracy is improved by approximately 50%. Using the identified dynamic model combined with the Jacobian matrix of the robot, the external force/torque at the end-effector of the robot is calculated in real time. The Kalman filter is used to filter the torque value to improve the calculation accuracy. Finally, the peg-in-hole insertion experiment is performed, and the compliant control strategy using the PD position control as the inner loop ensures the reliable positional accuracy of the insertion process. For the peg-in-hole assembly, three cases are described and analyzed in this paper. The fluctuation range of the force during assembly does not exceed 4N. Experiments show that the compliant control algorithm can achieve satisfactory flexibility of the robot to the external environment.

In the future work, if the rigid-body dynamic model is improved to be an elastic-body dynamic model, the precision of the external force/torque calculating algorithm will be better. The way to improve the dynamic model is one of the interesting problems and will be included in our future research works.

REFERENCES

[1] H. Chen, B. Zhang, and G. Zhang, *Handbook of Manufacturing Engineering and Technology*. London, U.K.: Springer, 2015, pp. 2347–2401.
[2] P. Aivaliotis, G. Michalos, and S. Makris, "Cooperating robots for fixtureless assembly: Modelling and simulation of tool exchange process," *Int. J. Comput. Integr. Manuf.*, vol. 31, no. 12, pp. 1235–1246, 2018.
[3] P. Aivaliotis, K. Georgoulias, and G. Chryssolouris, "A RUL calculation approach based on physical-based simulation models for predictive maintenance," in *Proc. Int. Conf. Eng. Technol. Innov. (ICE IEEE)*, Funchal, Portugal, Jun. 2017, pp. 1243–1246.
[4] D. I. Park, H. Kim, C. Park, T. Choi, H. Do, B. Kim, and J. Park, "Automatic assembly method with the passive compliant device," in *Proc. 11th Asian Control Conf. (ASCC)*, Gold Coast, QLD, Australia, Dec. 2017, pp. 347–348.
[5] Y. Zhao, N. Paine, S. J. Jorgensen, and L. Sentis, "Impedance control and performance measure of series elastic actuators," *IEEE Trans. Ind. Electron.*, vol. 65, no. 3, pp. 2817–2827, Mar. 2018.
[6] T. Yoshikawa, "Dynamic hybrid position/force control of robot manipulators–Description of hand constraints and calculation of joint driving force," *IEEE J. Robot. Autom.*, vol. JRA-3, no. 5, pp. 386–392, Oct. 1987.
[7] M. H. Raibert and J. J. Craig, "Hybrid position/force control of manipulators," *J. Dyn. Syst., Meas., Control*, vol. 103, no. 2, pp. 126–133, 1981.
[8] O. Khatib, "A unified approach for motion and force control of robot manipulators: The operational space formulation," *IEEE J. Robot. Autom.*, vol. 3, no. 1, pp. 43–53, Feb. 1987.

[9] A. Flores-Abad, A. Crain, M. Nandayapa, M. A. Garcia-Teran, and S. Ulrich, "Disturbance observer-based impedance control for a compliance capture of an object in space," in *Proc. AIAA Guid., Navigat., Control Conf.*, Kissimmee, Florida, 2018.
[10] B. Lukic and K. Jovanovic, "Influence of mechanical characteristics of a compliant robot on Cartesian impedance control design," in *Proc. 2nd IcETRAN Conf.*, Silver Lake, Serbia, 2015, pp. 1–6.
[11] Y. Li, S. S. Ge, Q. Zhang, and T. H. Lee, "Neural networks impedance control of robots interacting with environments," *IET Control Theory Appl.*, vol. 7, no. 11, pp. 1509–1519, 2013.
[12] N. Hogan, "Impedance control: An approach to manipulation: Part I—Theory," *J. Dyn. Syst., Meas., Control*, vol. 107, no. 1, pp. 1–7, 1985.
[13] H. Park, J. Park, D.-H. Lee, J.-H. Park, M.-H. Baeg, and J.-H. Bae, "Compliance-based robotic peg-in-hole assembly strategy without force feedback," *IEEE Trans. Ind. Electron.*, vol. 64, no. 8, pp. 6299–6309, Aug. 2017.
[14] A. Kramberger, A. Gams, B. Nemec, D. Chrysostomou, O. Madsen, and A. Ude, "Generalization of orientation trajectories and force-torque profiles for robotic assembly," *Robot. Auton. Syst.*, vol. 98, pp. 333–346, Dec. 2017.
[15] M. Focchi, G. A. Medrano-Cerda, T. Boaventura, M. Frigerio, C. Semini, J. Buchli, and D. G. Caldwell, "Robot impedance control and passivity analysis with inner torque and velocity feedback loops," *Control Theory Appl.*, vol. 14, no. 2, pp. 97–112, 2016.
[16] J. Su, R. Li, H. Qiao, J. Xu, Q. Ai, and J. Zhu, "Study on dual peg-in-hole insertion using of constraints formed in the environment," *Ind. Robot, Int. J.*, vol. 44, no. 6, pp. 730–740, 2017.
[17] J. Xiao, Q. Zhang, Y. Hong, G. Wang, and F. Zeng, "Collision detection algorithm for collaborative robots considering joint friction," *Int. J. Adv. Robot. Syst.*, vol. 15, no. 4, pp. 1–13, 2018.
[18] A. Flores-Abad, M. Nandayapa, and M. A. Garcia-Teran, "Force sensorless impedance control for a space robot to capture a satellite for on-orbit servicing," in *Proc. IEEE Aerosp. Conf.*, Big Sky, MT, USA, 2018, pp. 1–7.
[19] S. P. Chan and H. C. Liaw, "Generalized impedance control of robot for assembly tasks requiring compliant manipulation," *IEEE Trans. Ind. Electron.*, vol. 43, no. 4, pp. 453–461, Aug. 1996.
[20] J. Krüger, G. Schreck, and D. Surdilovic, "Dual arm robot for flexible and cooperative assembly," *CIRP Ann.*, vol. 60, no. 1, pp. 5–8, 2011.
[21] F. Caccavale, C. Natale, B. Siciliano, and L. Villani, "Six-DOF impedance control based on angle/axis representations," *IEEE Trans. Robot. Autom.*, vol. 15, no. 2, pp. 289–300, Apr. 1999.
[22] N. Rahimi, I. Howard, and C. Lei, "Neural impedance adaption for assistive human–robot interaction," *Neurocomputing*, vol. 290, pp. 50–59, May 2018.
[23] K. Kokkalis, G. Michalos, P. Aivaliotis, and S. Makris, "An approach for implementing power and force limiting in sensorless industrial robots," *Procedia CIRP*, vol. 76, pp. 138–143, May 2018.
[24] Y. Dong, T. Ren, K. Chen, and D. Wu, "An efficient robot payload identification method for industrial application," *Ind. Robot, Int. J.*, vol. 45, no. 4, pp. 505–515, Apr. 2018.
[25] C. Natale, R. Koeppe, and G. Hirzinger, "A systematic design procedure of force controllers for industrial robots," *IEEE/ASME Trans. Mechatronics*, vol. 5, no. 2, pp. 122–131, Jun. 2000.
[26] J. Maples and J. Becker, "Experiments in force control of robotic manipulators," in *Proc. IEEE Int. Conf. Robot. Automat.*, San Francisco, CA, USA, Apr. 1986, pp. 695–702.
[27] J. Xiao, F. Zeng, Q. Zhang, and H. Liu, "Research on the forcefree control of cooperative robots based on dynamic parameters identification," *Ind. Robot, Int. J. Robot. Res. Appl.*, vol. 46, no. 4 pp. 499–509, Jun. 2019. doi: 10.1108/IR-01-2019-0007.

FAN ZENG was born in 1995. He received the B.Sc. degree from Qiushi Honors College, Tianjin University, Tianjin, China, in 2017, where he is currently pursuing the M.Sc. degree with the School of Mechanical Engineering. His research interests include human–robots collaboration, dynamics of robots, force/position control, and compliant assembly.

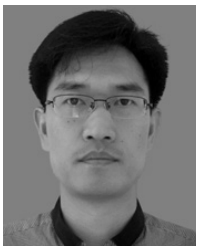

JULIANG XIAO was born in 1977. He received the Ph.D. degree from the School of Mechanical Engineering, Tianjin University, China, in 2006, where he is currently an Associate Professor. His research interests include collaborative robot, robotic control, intelligent manufacturing, mechatronic, and hydraulic integration.

HAITAO LIU was born in 1981. He received the Ph.D. degree from the School of Mechanical Engineering, Tianjin University, China, in 2010, where he is currently a Professor. His research interests include mechanisms and parallel manipulators.